Dinoop Lal S. "Photodegradation of polystyrene by nano titanium dioxide and photosensitizers." Thesis. Research & Postgraduate Department of Chemistry, St. Thomas' College (Autonomous), Thrissur, University of Calicut, 2020.

Chapter 7

Enhanced Photocatalytic Activity of Metal Doped TiO$_2$ for the UV degradation of Polystyrene

Abstract

UV degradation of PS was studied in the presence of metal doped TiO$_2$. Silver, iron and copper doped TiO$_2$ were prepared by sol-gel route in which the corresponding metal salts were added to the developing TiO$_2$ particles at pH 4. Metal doped TiO$_2$ with 3, 10 and 30 percentage of metals were prepared. XRD analysis revealed that as the percentage of metal doping increased, phase change occurred from anatase to rutile, easily at lower calcination temperature of 400°C. The photocatalytic activity of TiO$_2$ increased considerably upon metal doping, for the UV degradation of PS. Lower percentage metal doped TiO$_2$ acted as better photocatalyst compared to higher percent metal doped TiO$_2$. Ag doped TiO$_2$ showed enhanced photocatalytic efficiency compared to Fe or Cu doped TiO$_2$.

7.1. Introduction

The fate of photogenerated charges entirely determines the photocatalytic activity of TiO_2 which further depends upon its surface property. One of the methods employed for controlling the surface property of TiO_2 intrinsically is doping. Surface separation results as a consequence of doping where spatial trapping of photogenerated charge carriers take place. These spatially trapped charges are transferred to the associated substrates for redox reactions[1]. Metal doping has an advantage of introducing sub bands which are closer to the conduction band (CB) of TiO_2[2–4]. This is attained through the overlap of 3d orbital of titanium with suitable orbital of metals (*d*-orbitals in transition metals and *f*-orbitals in rare earth metals)[5]. An outcome of this interaction is the decrease in bandgap energies[6–8]. TiO_2 doped with noble metals including Pt[9], Pd[10], Ru[11], Rh[11], Ag[12], Au[13] etc have been reported to increase the photocatalytic efficiency by hindering the recombination of photogenerated electrons in conduction band (CB) and holes in valence band (VB). Schottky barrier that results at the interface of TiO_2 and metal explains the obstruction of these photogenerated charge recombination. Electrons from the CB of TiO_2 are captured by the noble metals which are stored and further transferred into another accepter associated with it initiating photochemical reaction. TiO_2 doped with other transition metals including Fe[14–16], Cu[17], Cr[14], Mn[14,18], Co[14], Ni[14,19], V[20], Zn[21] etc., also have been reported with superior photocatalytic activity. Charge transfer between CB or VB of TiO_2 and the *d*-orbitals of the transition metals changed the electronic structure causing a red shift in the absorption from UV to visible region.

In this chapter, photodegradation of PS is studied using TiO_2 doped with Ag, Cu and Fe transition metals. TiO_2 doped with Ag, Cu and Fe as photocatalysts have already been used in various applications and satisfying results were obtained. Fe doped TiO_2 has been used as photocatalyst in the degradation of organic dyes like methyl orange[22,23], reactive blue 4[24], azo fuchsine[25], XRG[26], phenol[27] etc. Cu doped TiO_2 was reported to catalyse the degradation of methyl orange[28], nitrates[29] etc. The application of thin film of Cu doped TiO_2 which is super hydrophilic has been reported to exhibit anti-fogging property under sun light[30]. The antimicrobial activity of Cu doped TiO_2 photocatalyst has also been reported[31]. The degradation of dyes including azo dye[32], direct red 23[33], basic violet[34] etc has been reported using Ag

doped TiO_2 as photocatalyst. The degradation of chloroform and urea using Ag doped TiO_2 catalyst exhibited superior activity compared to pure TiO_2[35].

Section:I

Synthesis and characterisation of metal doped TiO_2

7.2. Experimental

7.2.1. Synthesis of Ag Doped TiO_2

Ag doped TiO_2 was prepared using sol-gel technique. Titanium (IV) isopropoxide (TTIP) was used as precursor of TiO_2 and silver nitrate ($AgNO_3$) for Ag. In order to prepare TiO_2 with 3 mole percentage of Ag, 2.463 g of TTIP (2.57 ml) was added to 14 ml ethanol and stirred at 4°C using a magnetic stirrer (solution I) for one hour. Meanwhile 0.054 g of $AgNO_3$ was dissolved in 4ml distilled water (solution II). Solution II was then added dropwise into solution I while stirring. The pH of the system was adjusted to 4 using drops of nitric acid. The system was stirred for three more hours. The colloidal solution hence obtained was filtered and washed using ethanol followed by distilled water. The resulting gel was dried at 120°C for 6 hours. The grey powder hence obtained was calcinated at 400°C for 5 hours[36].

In a similar way, TiO_2 doped with 10 and 30 mole percentages of Ag were also prepared. The composites were named as TiO_2-3% Ag, TiO_2-10% Ag and TiO_2-30% Ag depending on the mole percentage of Ag versus TiO_2 in the composites. Table 7.1.1 below represents the details of prepared Ag doped TiO_2 composites.

Table 7.1.1. *TiO₂-Ag composites*

Composite	TiO₂ Mole %	Ag Mole %	Weight of AgNO₃ (g)	Weight of TTIP (g)
TiO₂+3% Ag	97	3	0.0537	2.4630
TiO₂+10% Ag	90	10	0.1794	2.8206
TiO₂+30% Ag	70	30	0.5381	2.4619

7.2.2. Synthesis of Fe Doped TiO$_2$

Fe doped TiO$_2$ was prepared via sol-gel route. TTIP served as the precursor for TiO$_2$ and Iron (III) nitrate nonahydrate (Fe(NO$_3$)$_3$.9H$_2$O) for Fe in the composite. For the preparation of 3 mole percent Fe doped TiO$_2$, 2.872 g TTIP (2.99 ml) was dissolved in 14 ml ethanol and stirred at 4°C using a magnetic stirrer (solution I). Solution II consisting of 0.128 g Fe(NO$_3$)$_3$.9H$_2$O dissolved in 4 ml distilled water was added dropwise into solution I. pH of the solution was adjusted to 4 using nitric acid followed by three hours of stirring. The resulting product was filtered and washed using ethanol followed by water. The gel obtained was dried at 120°C for 6 hours. The reddish brown powder hence obtained was calcinated at 400°C for 5 hours[22,37].

10 and 30 mole percentages of Fe doped TiO$_2$ were also prepared in a similar manner to obtain TiO$_2$-10% Fe and TiO$_2$-30% Fe. The details of the prepared TiO$_2$-Fe composites are as tabulated below (Table 7.1.2).

Table 7.1.2. TiO$_2$-Fe composites

Composite	TiO$_2$ Mole %	Fe Mole %	Weight of Fe(NO$_3$)$_3$.9H$_2$O (g)	Weight of TTIP (g)
TiO$_2$+3% Fe	97	3	0.128	2.872
TiO$_2$+10% Fe	90	10	0.427	2.573
TiO$_2$+30% Fe	70	30	1.280	1.720

7.2.3. Synthesis of Cu Doped TiO$_2$

Preparation of Cu doped TiO$_2$ was also done via sol-gel method as discussed above. Copper sulphate pentahydrate (CuSO$_4$.5H$_2$O) was used as the precursor for Cu in TiO$_2$-Cu composites. In order to prepare 3 mole percentage Cu doped TiO$_2$ (namely TiO$_2$-3%Cu), 2.949 g TTIP (3.066 ml) was dissolved in 14 ml ethanol and stirred at 4°C using a magnetic stirrer (solution I). 0.051g CuSO$_4$.5H$_2$O dissolved in 4ml distilled water (solution II) was added to solution I, dropwise. The system was adjusted to pH 4 using nitric acid and stirred for three hours. The resulting product was filtered, washed and dried at 120°C for 6 hours. The pale blue solid powder was calcinated at 400 °C for 5 hours[8].

TiO$_2$ doped with 10 mole percentage and 30 mole percentage of Cu were also prepared (named as TiO$_2$-10% Cu and TiO$_2$-30% Cu). The details of the prepared TiO$_2$-Cu composites are as tabulated below (Table 7.1.3).

Table 7.1.3. TiO$_2$-Cu composites

Composite	TiO$_2$ Mole %	Cu Mole %	Weight of CuSO$_4$.5H$_2$O (g)	Weight of TTIP (g)
TiO$_2$+3% Cu	97	3	0.051	2.949
TiO$_2$+10% Cu	90	10	0.169	2.831
TiO$_2$+30% Cu	70	30	0.506	2.494

The prepared TiO$_2$-Cu, TiO$_2$-Ag and TiO$_2$-Fe composites were characterized using various techniques and results are discussed below.

7.3. Results and discussion

7.3.1. Powder XRD
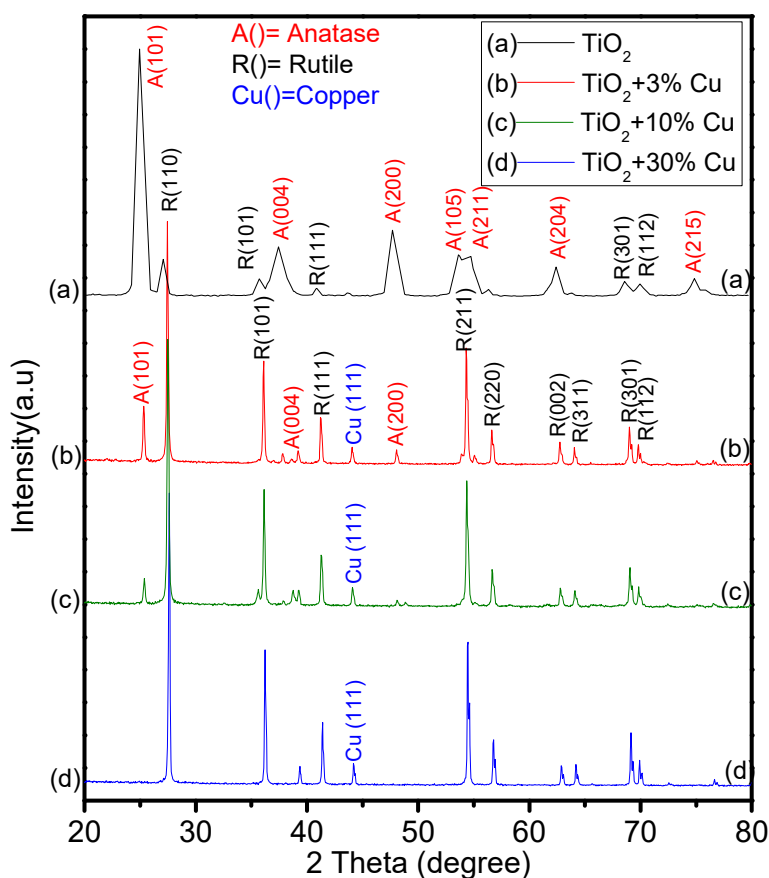
Figure 7.1.1. XRD pattern of TiO$_2$ –Cu composites

Higher percentage of metal doping in TiO_2 favoured its phase change from anatase to rutile at a calcination temperature of 400°C for 5 hours. The XRD pattern of metal doped TiO_2-3% Cu composite exhibited the peaks corresponding to anatase and rutile phases (Figure 7.1.1). The peaks observed at $2\theta = 25.3°$ (101), 37.8° (004) and 48.05° (200) attributes to anatase phase and peaks at $2\theta = 27.45°$ (110), 36.09° (101), 41.22° (111), 54.3 (211), 56.62 (220), 62.74 (002), 69.0 (301) and 69.79° (112) attributes to the rutile phase of TiO_2 existing in the composite. In addition to these, a new peak at $2\theta = 44.05°$ corresponding to $C\overset{o}{u}$ (111) plane was also observed. On comparing the results with the XRD pattern of pristine TiO_2 (Figure 7.1.1 a), it is evident that the intensity of the peaks corresponding to the anatase phase decreased with an increase in the peak intensities of rutile phase. Some of the peaks corresponding to anatase phase were absent. On further increasing the metal doping percentage (TiO_2-10% Cu), the peak intensities corresponding to anatase phase decreased further. In TiO_2-30% Cu composite, TiO_2 existed almost in rutile phase.

Percentage of anatase and rutile phases of TiO_2 existing in the composites were determined by Spurr equations (equation 7.1 and 7.2)[38].

Percentage of anatase phase, $A\% = 100 \Big/ \left\{ 1 + 1.265 \left(\frac{I_R}{I_A} \right) \right\}$ (7.1)

Percentage of rutile phase, $R\% = 1 \Big/ \left\{ 1 + 0.8 \left(\frac{I_A}{I_R} \right) \right\}$ (7.2)

Where I_A represents the intensity of anatase (101) peak and I_R represents the rutile (110) peak. Table 7.2.1 represents the percentage of anatase and rutile phases of TiO_2-Cu composites.

Table 7.2.1. Percentage of anatase and rutile phases in TiO₂-Cu composites

	A% (101)	R%(110)
TiO₂	91.8	8.2
TiO₂+3% Cu	11.6	88.4
TiO₂+10% Cu	06.9	93.1
TiO₂+30% Cu	0	100

It should be noted that the values of A% and R% may not be accurate as the calculations were done considering only the anatase (101) and rutile (110) peaks observed in the XRD patterns.

Table 7.2.1 above clearly establishes the fact that the calcination temperature required for the phase transition from anatase to rutile phase of TiO_2 decreased upon Cu incorporation. Pristine TiO_2 which existed in ~91.8% anatase and ~8.2% rutile phase after calcination at 400° C for 5 hours have almost been converted into ~100% rutile form at the same calcination temperature upon 30% Cu incorporation.

Crystallite size of TiO_2-Cu composites calculated from the most prominent peak of the diffractogram was larger compared to that of pristine TiO_2 as determined through Debye Scherrer's equation (Table 7.2.2). The crystallite size increases as the percentage of Cu doping increases in the composites.

Table 7.2.2. Tabulated values of crystallite size of TiO_2-Cu composites

	Crystallite size (nm)
TiO₂	18.9
TiO₂+3% Cu	47.0
TiO₂+10% Cu	50.7
TiO₂+30% Cu	56.2

The observations made from the XRD pattern of TiO_2-Ag composites (Figure 7.1.2) were much similar to that of TiO_2-Cu composites. The increase in the percentage of Ag doping in TiO_2 leads to a gradual phase change from anatase to rutile at the calcination temperature of 400°C for 5 hours. In addition to the diffraction patterns corresponding to the predominant rutile and trace anatase phase, diffraction patterns were also observed at 2θ=38.3° and 44.4° which could be attributed to (111) and (200) planes of Ag. These peak intensities increased as the percentage of Ag doping in the composites increased. The percentage of anatase (A %) and rutile (R %) in the composites calculated using Spurr equations (equations 7.1 & 7.2) are tabulated in Table 7.2.3. The crystallite size of the composites was found to be larger than that of pristine TiO_2 as determined through Debye Scherrer's equation. An increase in the crystallite size among the composites was observed as the percentage of Ag doping increased (Table 7.2.4).
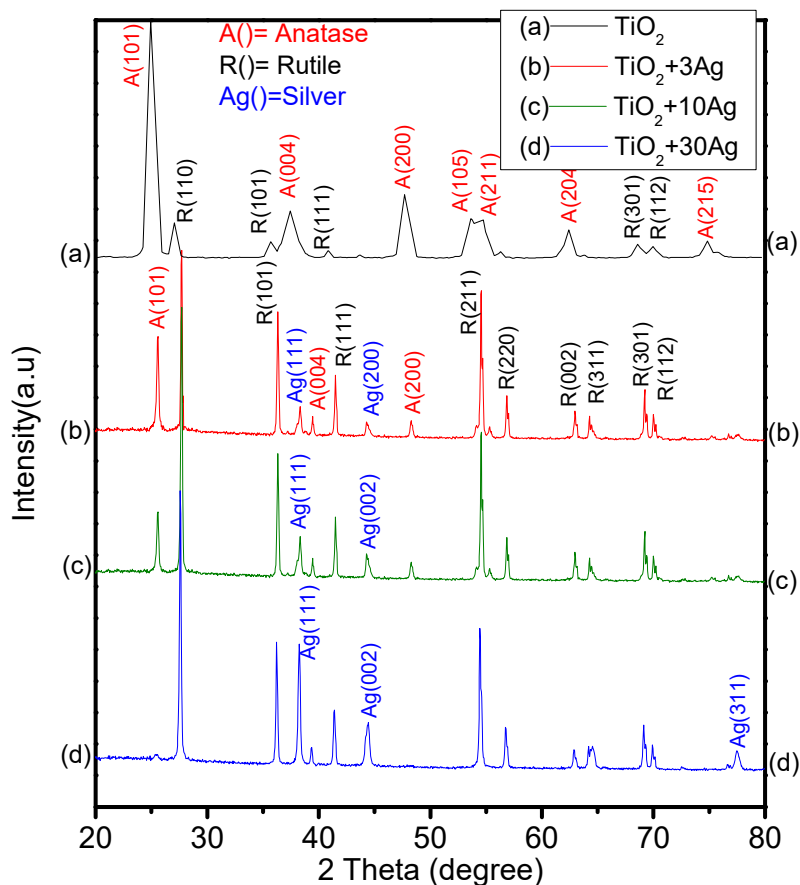
Figure 7.1.2. *XRD pattern of TiO₂ –Ag composites*

Table 7.2.3. *Percentage of anatase and rutile phases in TiO₂-Ag composites*

	A% (101)	*R%(110)*
TiO₂	91.8	8.2
TiO₂+3% Ag	29.3	70.7
TiO₂+10% Ag	15.6	84.4
TiO₂+30% Ag	0	100

Table 7.2.4. *Values of crystallite size of TiO₂-Ag composites*

	Crystallite size (nm)
TiO₂	18.9
TiO₂+3% Ag	46.6
TiO₂+10% Ag	51.1
TiO₂+30% Ag	62.7
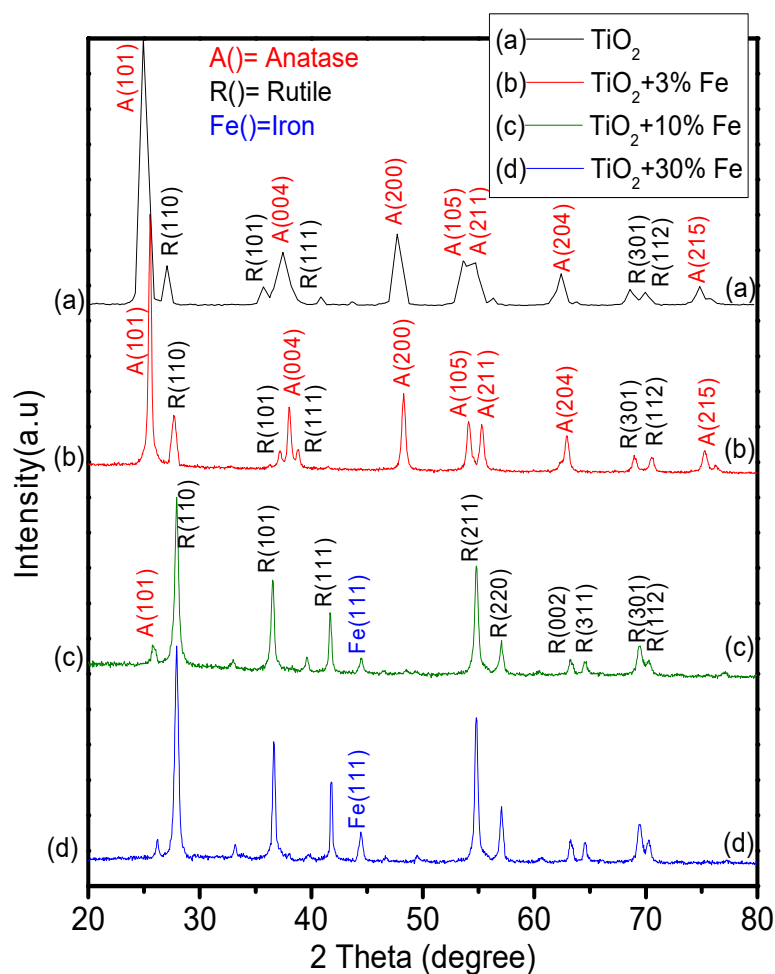
***Figure 7.1.3**. XRD pattern of TiO₂ –Fe composites*

The diffraction patterns of the TiO₂-Fe composites (Figure 7.1.3) exhibited a slight variation from that of TiO₂-Cu and TiO₂-Ag composites. TiO₂-3% Fe exhibited similar diffraction patterns as observed in pristine TiO₂. Anatase phase is predominated over rutile phase here. Peaks corresponding to Fe were not observed. As the percentage of Fe is increased in the composites (ie, TiO₂-10% Fe & TiO₂-30% Fe) the phase change from anatase to rutile is observed. In addition to this, the peak corresponding to Fe° (111) at $2\theta=44.45°$ is also observed. The percentage of anatase (A%) and rutile (R %) calculated using Spurr equations are tabulated in table 7.2.5. The crystallite size of the TiO₂-Fe composites were larger compared to that of pristine TiO₂. Increased percentage of Fe doping further increases the crystallite size of the particles among the TiO₂-Fe composites which is tabulated below (Table 7.2.6).

Table 7.2.5. *Percentage of anatase and rutile phases in TiO₂-Fe composites*

	A% (101)	R%(110)
TiO₂	91.8	8.2
TiO₂+3% Fe	79.2	20.8
TiO₂+10% Fe	9.3	90.7
TiO₂+30% Fe	6.7	93.3

Table 7.2.6. *Values of crystallite size of TiO₂-Fe composites*

	Crystallite size (nm)
TiO₂	18.9
TiO₂+3% Fe	21.2
TiO₂+10% Fe	27.6
TiO₂+30% Fe	29.8

As discussed earlier, TiO_2-3% Fe composite existed predominantly in the anatase phase (~79.2% anatase and ~20.8% rutile) and the peak corresponding to Fe was absent. TiO_2-3% Cu and TiO_2-3% Ag composites, on the other hand, existed predominantly in the rutile phase. The peaks corresponding to $\overset{o}{Cu}$ (111) and $\overset{o}{Ag}$ (111) were present in the XRD pattern of their respective composites. This observation reveals the fact that more Fe^{3+} ions originating from $Fe(NO_3)_3.9H_2O$ precursor might have replaced the Ti^{4+} ions from the crystal frame work of anatase TiO_2 more actively compared to that of Ag^+ or Cu^{2+} ions originating from $AgNO_3$ or $CuSO_4.5H_2O$ precursors respectively. In such cases where Fe^{3+} ion replaces the Ti^{4+} ion from the anatase TiO_2 lattice, the phase remains unaltered and the diffraction patterns corresponding to Fe^{3+} may not be observed. Radius of Ti^{4+} ion (~0.64 Å) being almost similar to that of Fe^{3+} ion (~0.64Å), the latter can easily replace Ti^{4+} ions from its crystal lattice. As the percentage of Fe doping is increased from 10% to 30%, phase change of TiO_2 from anatase to rutile was enhanced without elevating the calcination temperature (400°C). The peak corresponding to $\overset{o}{Fe}$ (111) was also observed. The observed peak for Fe could arise due to the reduction of agglomerated Fe^{3+} ions on the surface of TiO_2 [39].
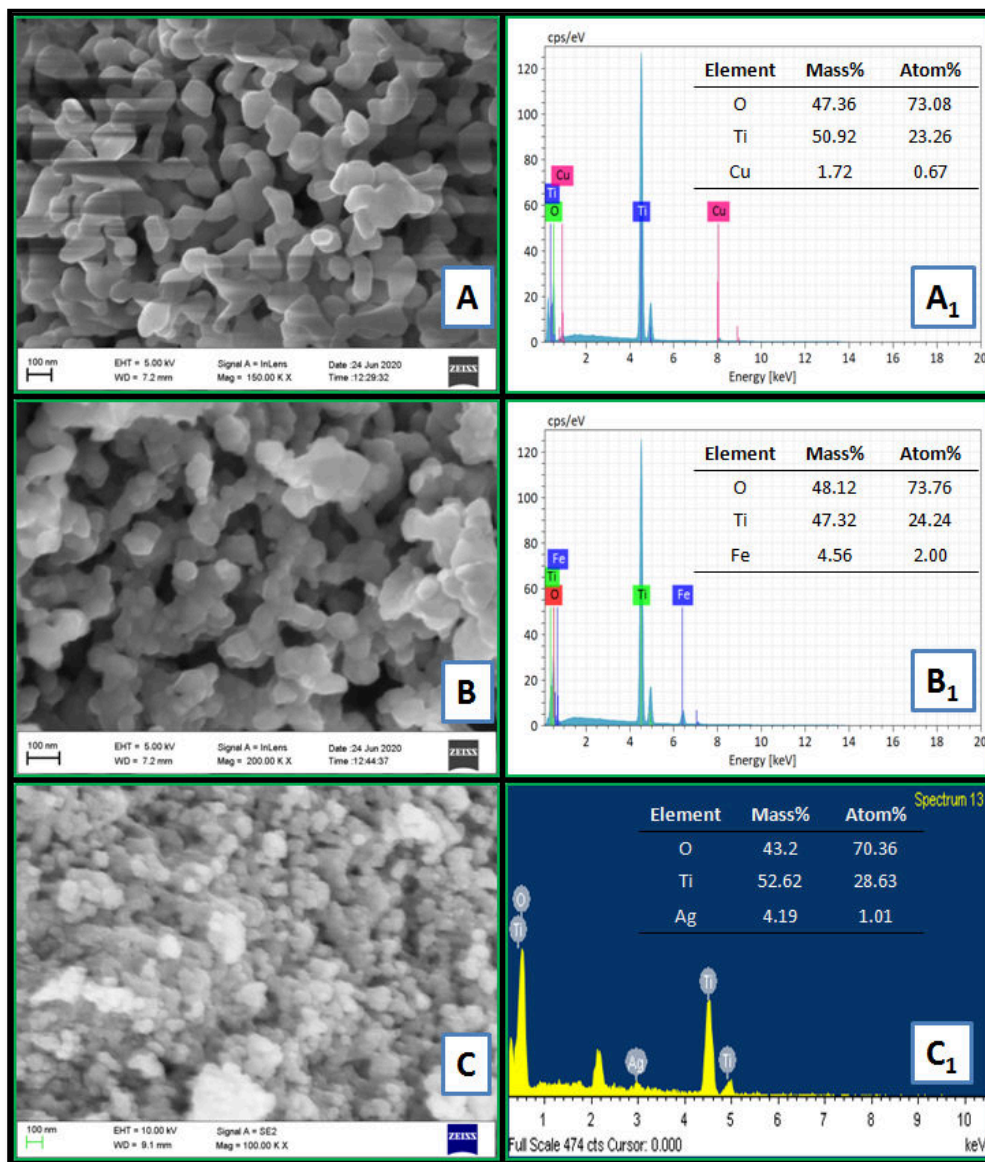
7.3.2. FESEM-EDX analysis

***Figure 7.2**. FESEM image and EDX spectra of TiO$_2$ –3% Cu (A & A$_1$), TiO$_2$ –3% Fe (B & B$_1$) and TiO$_2$ –3% Ag (C & C$_1$) composites.*

FESEM image of TiO$_2$-3% Cu (Figure 7.2 A) revealed its sphere like particle morphology with average particle diameter ~125 nm. EDX pattern of the composite (Figure 7.2 A$_1$) showed the presence of titanium at 4.51 (Kα1), 4.93 (Kβ1) and 0.45 (Lα1) keV and oxygen at 0.53 (Kα1) keV. The presence of copper was observed at 0.93 (Lα1), 0.95 (Lβ1), 8.03 (Kα1), 8.05 (Kα2), 8.91 (Kβ1) and 8.98 (Kβ2) keV. The absence of other elements confirmed the purity of the composite. TiO$_2$-3% Fe composite too existed as sphere like particles with an average particle diameter of 85 nm (Figure 7.2 B). EDX pattern of TiO$_2$-3% Fe (Figure 7.2 B$_1$) showed the presence

of iron at 0.71 (Lα1), 0.72 (Lβ1), 6.4 (Kα1 and Kα2 overlap) and 7.16 (Kβ1) keV in addition to titanium and oxygen with no other impurities. TiO_2-3% Ag composite existed as spherical particles with particle diameter ~50 nm as evident from its FESEM (Figure 7.2 C). EDX spectra of TiO_2-3% Ag composite indicates the presence of Ag at around 3 keV (Lα1, Lβ1 and Lβ2 overlap) along with titanium and oxygen without the presence of other elements (Figure 7.2 C_1).

7.3.3. FTIR spectroscopy

FTIR spectra of all the composites looked alike irrespective of the metal doping percentage or the type of metal used. It could be seen that the bands between 950 and 500 cm^{-1} corresponding to Ti-O/ Ti-O-Ti vibrations shifted towards lower wave number in all the metal doped TiO_2 composites compared to pristine TiO_2. Bands between 3600 and 3000 cm^{-1} corresponding to -OH stretching as well as bands at around 1680 cm^{-1} attributing H-O-H bending vibrations could also be observed from the FTIR spectra of the composites.
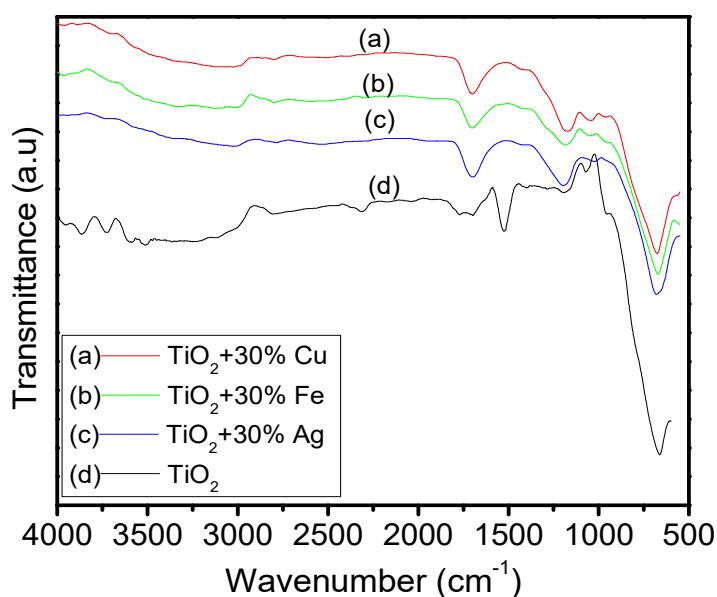

Figure 7.3. *FTIR image of TiO$_2$ –30% Cu (a), TiO$_2$ –30% Fe (b) and TiO$_2$ –30% Ag (c) composites.*

7.3.4. UV-visible diffused reflectance spectroscopy (UV-DRS)

Absorption spectra of TiO_2-Cu (Figure 7.4.1 A), TiO_2-Fe (Figure 7.4.2 A) and TiO_2-Ag (Figure 7.4.3 A) composites exhibited their absorption maxima in the UV region. Increased percentage of metal doping lead to an increase in the intensity of

absorption bands observed in the visible region. Optical bandgap energies (E_g) of the composites were determined by the application of Kubelka-Munk functions in Tauc plot.
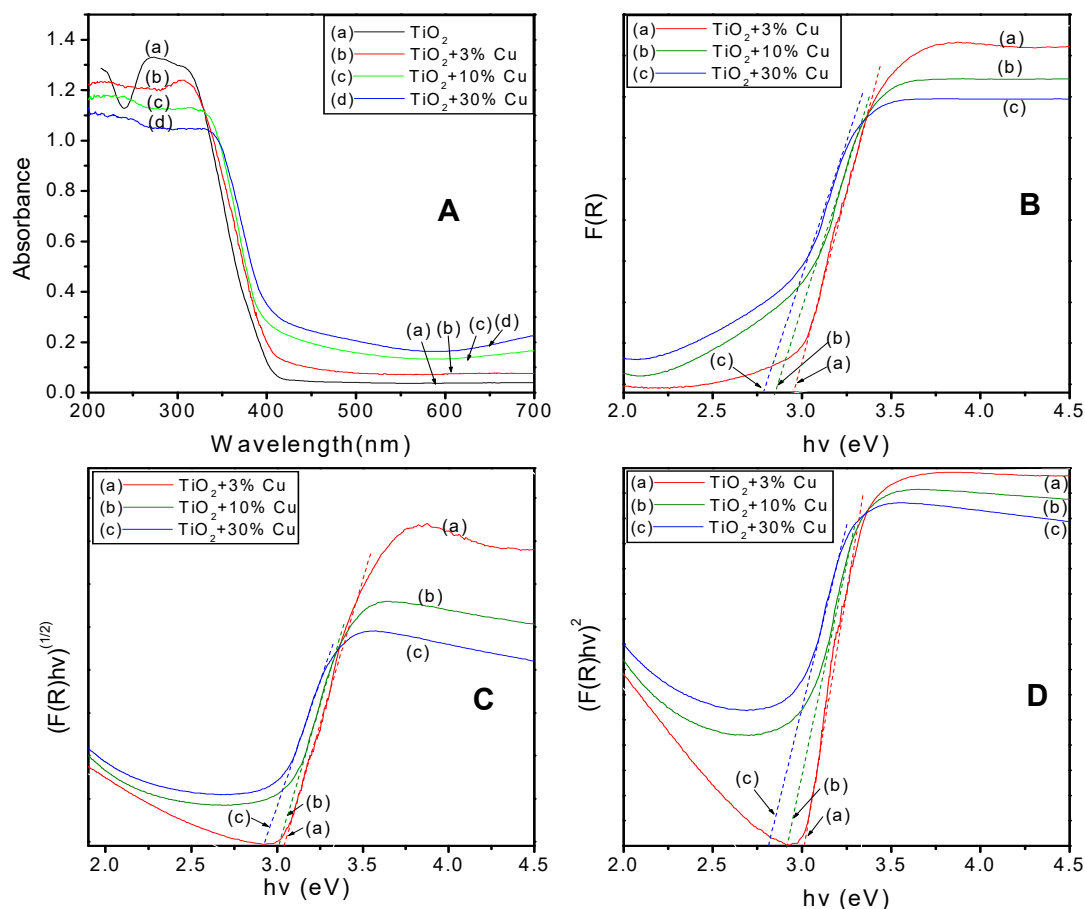

Figure 7.4.1. *Absorption spectra (A), F(R) versus hυ (B), (F(R)hυ)$^{1/2}$ versus hυ (C) and (F(R)hυ)^2 versus hυ (D) of TiO₂-Cu composites.*

Figure 7.4.1 B, C & D represents the E_g irrespective of transitions, indirect E_g and direct E_g of TiO₂-Cu composites respectively. Increase in the percentage of Cu doping lowered the E_g of the composites as represented in table 7.3.1.

Table 7.3.1. *Optical bandgap energies (E_gs) of TiO₂ –Cu composites*

Method	Transition Type	Optical Bandgap energy in eV			
		TiO_2	TiO_2- 3% Cu	TiO_2- 10% Cu	TiO_2- 30% Cu
F(R) vs hυ	Irrespective of transitions	3.16	2.97	2.85	2.78
(F(R)hυ)^2 vs hυ	Direct allowed	3.22	3.01	2.91	2.81
(F(R)hυ)$^{1/2}$ vs hυ	Indirect allowed	3.18	3.04	3.00	2.92
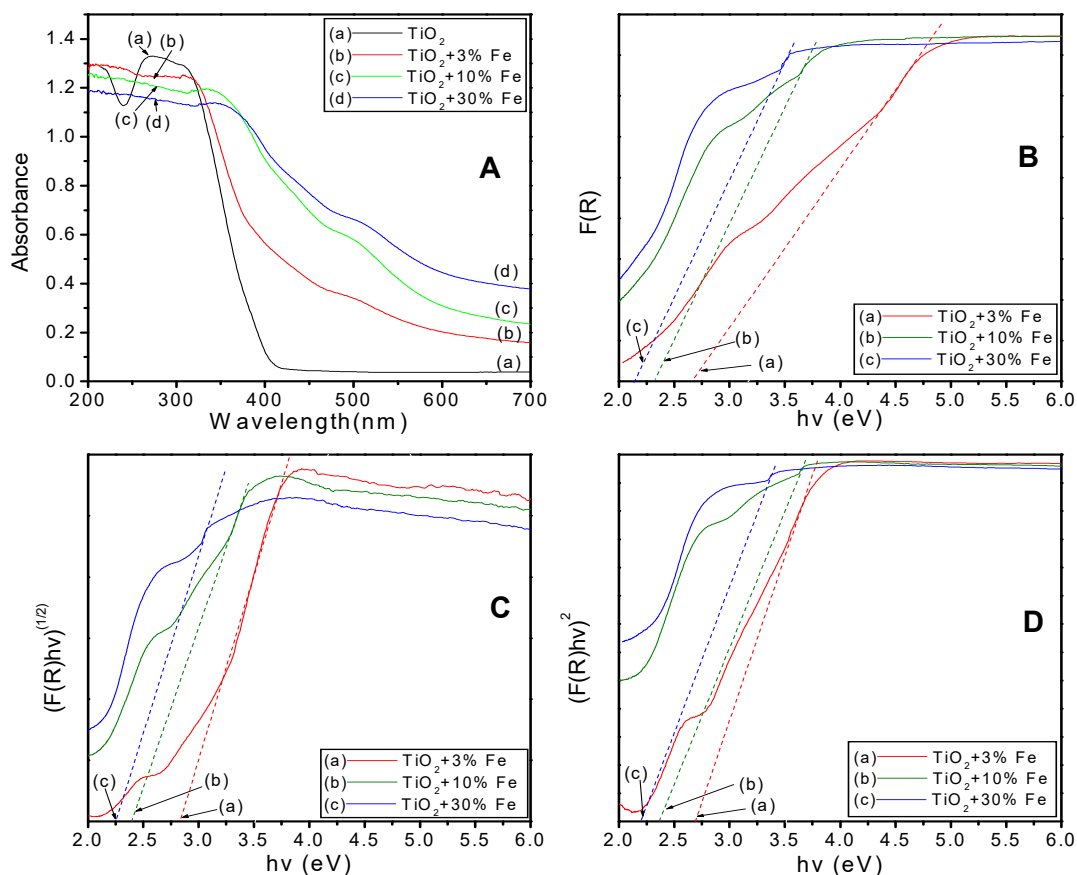
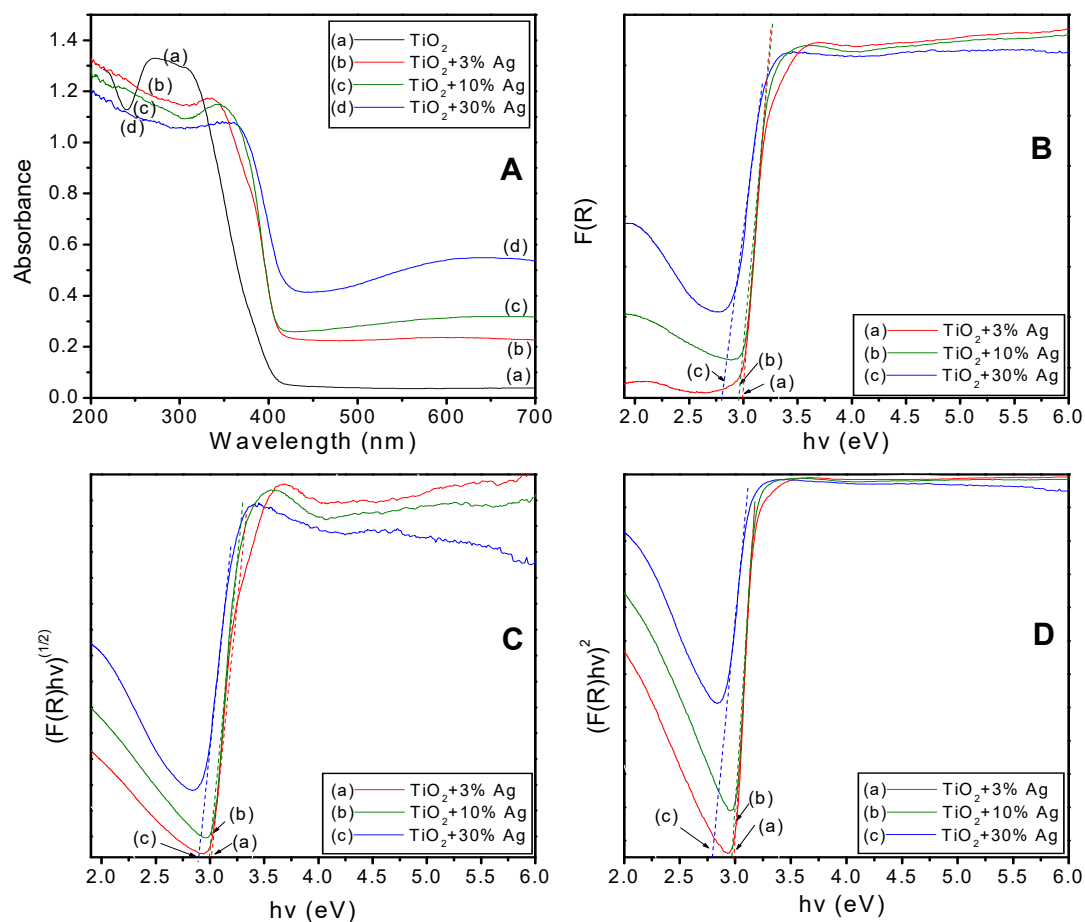*Figure 7.4.2*. Absorption spectra (A), F(R) versus hυ (B), (F(R)hυ)^{1/2} versus hυ (C) and (F(R)hυ)^2 versus hυ (D) of TiO_2-Fe composites.

The plots of E_g irrespective of transitions (Figure 7.4.2 B), indirect E_g (Figure 7.4.2 C) and direct E_g (Figure 7.4.2 D) of TiO_2-Fe composites showed a decrease in the values of E_g as the percentage of Fe doping increased. The values of Eg determined using the three methods are as tabulated in Table 7.3.2.

Table 7.3.2. Optical bandgap energies (E_gs) of TiO_2 –Fe composites

Method	Transition Type	Optical bandgap energy in eV			
		TiO_2	TiO_2-3% Fe	TiO_2-10% Fe	TiO_2-30% Fe
F(R) vs hυ	Irrespective of transitions	3.16	2.67	2.32	2.14
$(F(R)hυ)^2$ vs hυ	Direct allowed	3.22	2.83	2.39	2.26
$(F(R)hυ)^{1/2}$ vs hυ	Indirect allowed	3.18	2.69	2.36	2.20

Figure 7.4.3. *Absorption spectra (A), F(R) versus hυ (B), (F(R)hυ)$^{1/2}$ versus hυ (C) and (F(R)hυ)^2 versus hυ (D) of TiO$_2$-Ag composites.*

The E$_g$ values of TiO$_2$-Ag composites also decreased as the percentage of Ag doped increases as evident from the plots (Figure 7.4.3 B, C & D) and Table 7.3.3

Table 7.3.3. *Optical bandgap energies (E$_g$s) of TiO$_2$ –Ag composites*

Method	Transition Type	Optical bandgap energy in eV			
		TiO$_2$	TiO$_2$-3% Ag	TiO$_2$-10% Ag	TiO$_2$-30% Ag
F(R) vs hυ	Irrespective of transitions	3.16	2.99	2.96	2.80
(F(R)hυ)^2 vs hυ	Direct allowed	3.22	2.99	2.97	2.81
(F(R)hυ)$^{1/2}$ vs hυ	Indirect allowed	3.18	3.01	2.99	2.89

Section:II

Photodegradation of PS using metal doped TiO$_2$

7.4. Method

The synthesised, various metal doped TiO$_2$ were loaded into the PS matrix as discussed in chapter 2, and photodegradation of the resulting composites were studied. PS-TiO$_2$-metal composite specimens were also prepared for mechanical and electrical measurements. Photodegradation was monitored using various techniques and the obtained results are presented below.

7.5. Results and Discussion

Various monitoring techniques adopted in our study proved that PS-TiO$_2$-metal composites underwent better photodegradation in the presence of UV radiation compared to PS-TiO$_2$ composites. It was however noticed that increase in the percentage of metal doping in the composites could not increase the extent of photodegradation under UV light. Based on the results obtained, TiO$_2$ doped with 3 percentages of metals could be considered as better photocatalysts for the degradation of PS under UV radiation.

7.5.1. Gel permeation chromatography (GPC)

A decrease in the average molecular weights ($\overline{M}_w$ and $\overline{M}_n$) upon UV irradiation was observed in PS loaded with metal doped TiO$_2$ composites containing 3, 10 and 30% of metal compared to pristine TiO$_2$. PS-TiO$_2$-metal composites underwent better decrease in the average molecular weights in the presence of UV radiation compared to PS-TiO$_2$ composites. The extent of decrease in $\overline{M}_w$ and $\overline{M}_n$ of PS-TiO$_2$-Ag, PS-TiO$_2$-Fe and PS-TiO$_2$-Cu composites were almost similar. PS-TiO$_2$-Ag however underwent better decrease in $\overline{M}_w$ and $\overline{M}_n$ compared to PS-TiO$_2$-Fe and PS-TiO$_2$-Cu (Figure 7.5.1).
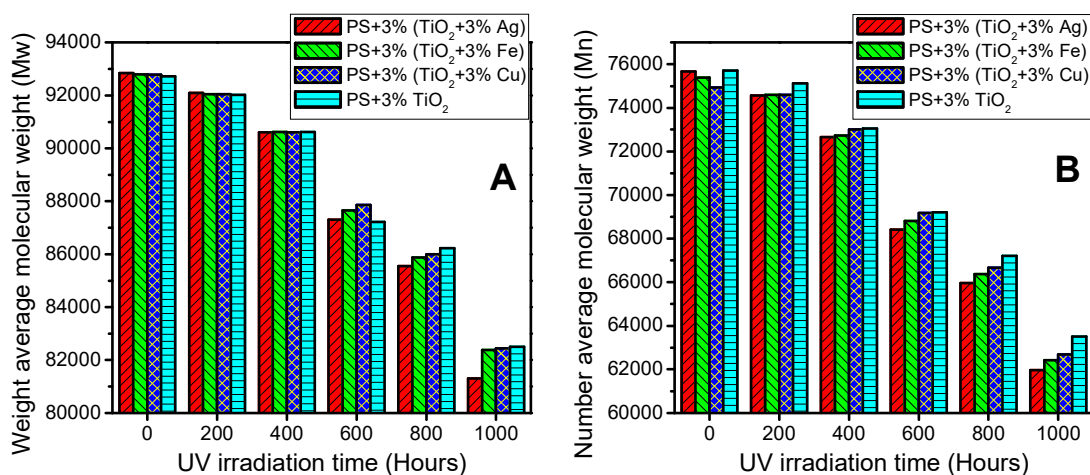
Figure 7.5.1. A) Weight average ($\bar{M}_w$) and B) number average ($\bar{M}_n$) molecular weights of PS-TiO₂-metal composites under different UV irradiation time
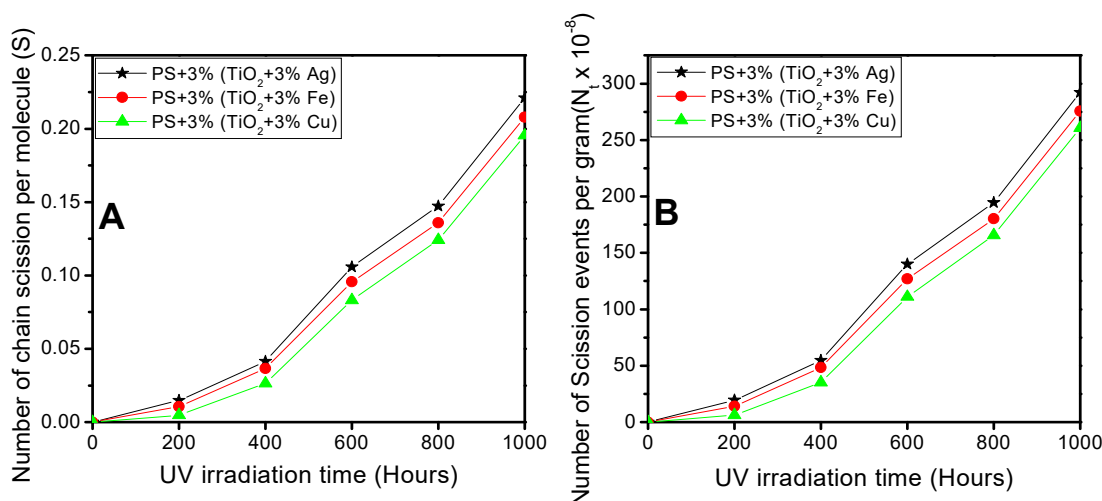

Figure 7.5.2. A) Number of chain scissions per molecule (S) and B) number of scission events per gram (Nₜ) of PS-TiO₂-metal composites under different UV irradiation time intervals

Number of chain scission per molecule (S) and number of scission events per gram (N_t) of the composites increased with UV irradiation time. From figure 7.5.2, it could be seen that the extent of chain scissions differed only by a very small value among PS-TiO₂-Ag, PS-TiO₂-Fe and PS-TiO₂-Cu composites. Extent of chain scission was however better in PS-TiO₂-Ag composite compared to others under study.
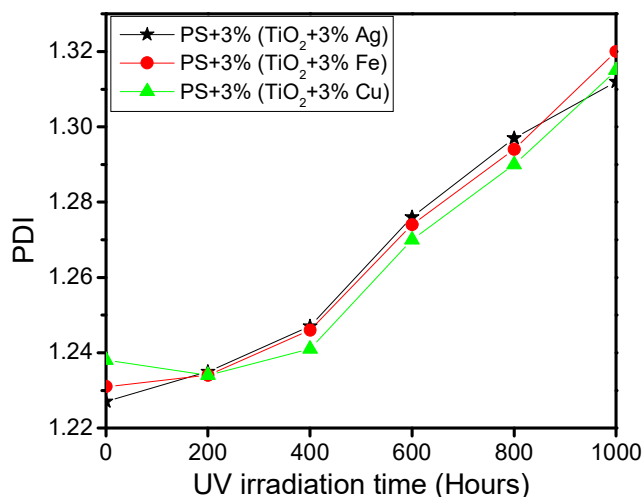
Figure 7.5.3. *Polydispersity index (PDI) of PS-TiO₂-metal composites under different UV irradiation time*

Polydispersity index (PDI) of all the PS-TiO$_2$-metal composites increased as the time of UV irradiation increases (Figure 7.5.3). The increase in the extent of random mannered chain scission due to photodegradation is evident here.
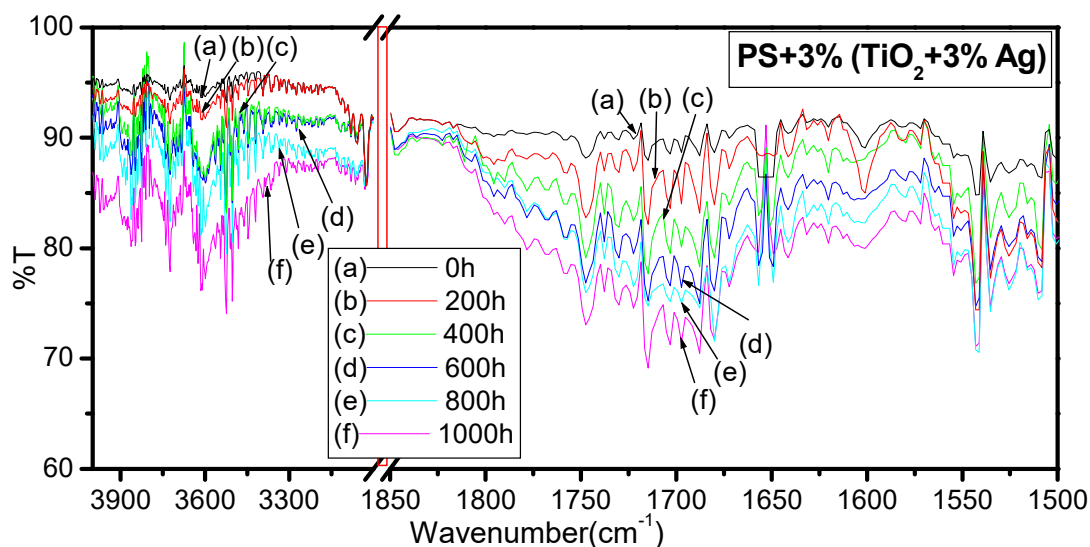
7.5.2. FTIR Spectroscopy

Figure 7.6. *FTIR spectra of PS-3%(TiO₂-3% Ag) at different UV exposure time intervals ranging from 0 h to 1000 h.*

FTIR spectra of all the PS-TiO$_2$-metal composites looked alike. An increase in the intensity of stretching vibrations corresponding to >C=O (1740-1700 cm^{-1}),   -OH/-OOH (3700-3600 cm^{-1}), >C=C< (1680-1650 cm^{-1}) etc were observed with the increase in UV irradiation time for all the composites. Photo-oxidation of the

composites taking place upon UV irradiation was evident. PS-TiO$_2$-metal composites underwent better photo-oxidation compared to PS-TiO$_2$ composites. Photo-oxidation taking place in PS-TiO$_2$-Ag composites (Figure 7.6) was slightly better compared to the other composites.

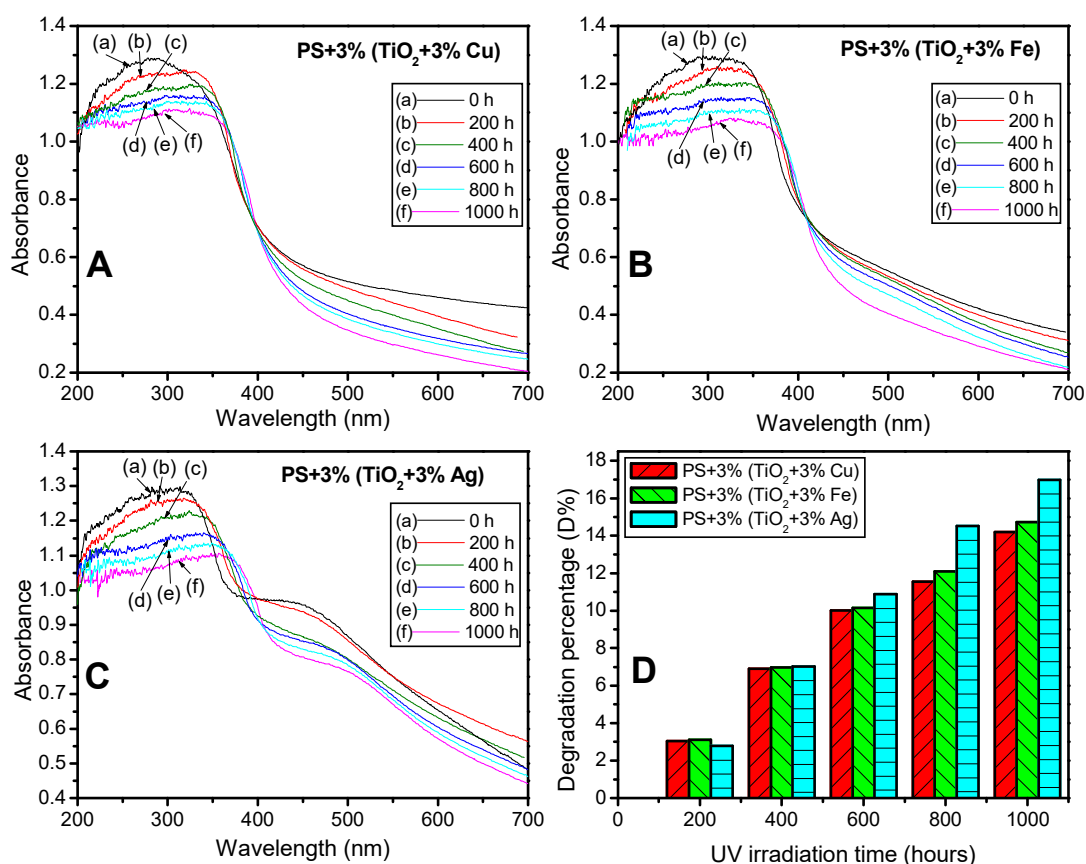### 7.5.3. UV-visible diffused reflectance spectroscopy (UV-DRS)

Figure 7.7. *UV-visible absorption spectra of PS-3%(TiO$_2$-3%Cu)* *(A)*, *PS-3%(TiO$_2$-3%Fe)* *(B)*, *PS-3%(TiO$_2$-3% Ag)* *(C)* *and degradation percentages of PS-(TiO$_2$-3% metal) composites* *(D)* *at different UV exposure time intervals ranging from 0 h to 1000 h*

PS-TiO$_2$-metal composites absorbed both in the UV and visible regions (Figure 7.7) unlike PS-TiO$_2$ composites which absorbed only in the UV region of the spectra. This indicates the possibility that the composites may utilise both UV and visible radiation to undergo photodegradation which has to be studied. The absorption maxima of the composites observed in the UV region decreased, as the time of UV irradiation increased pointing photodegradation possibility. A red shift was observed for the absorption bands in UV region indicating the formation of extended conjugation within the composites as a consequence of photodegradation. The

degradation percentage (D%) determined from UV-DRS were found to be maximum in PS-TiO$_2$-Ag composites compared to the PS composites with Fe or Cu doped TiO$_2$. The increase in degradation efficiency of PS-(TiO$_2$-3% Ag), PS-(TiO$_2$-3% Fe) and PS-(TiO$_2$-3% Cu) with respect to pristine PS were 7.37, 5.1 and 4.57 % respectively.
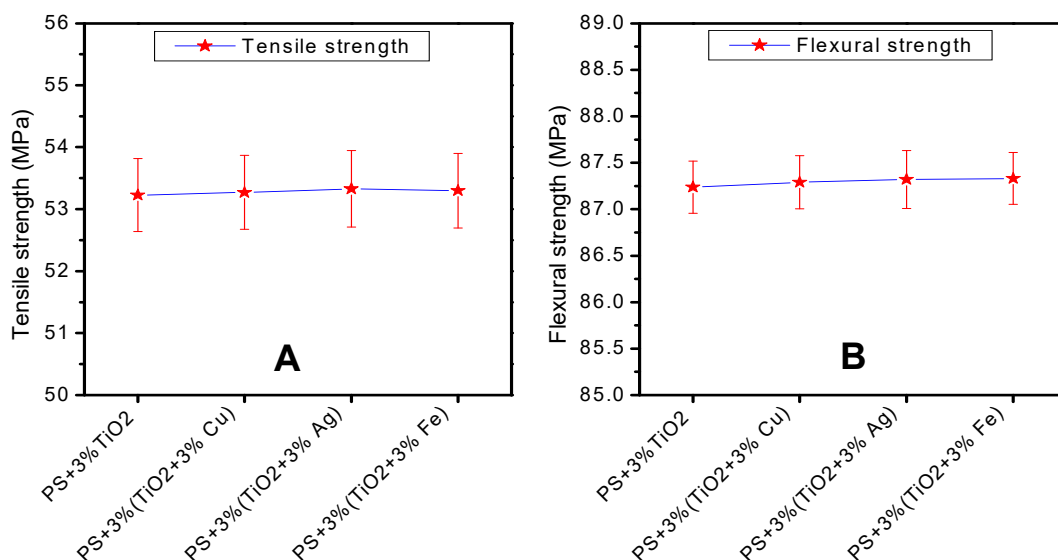
7.5.4. Mechanical Properties

Figure 7.8.1. *Tensile (A) and flexural (B) strengths of PS-TiO$_2$-metal and PS-TiO$_2$ composites-a comparison*
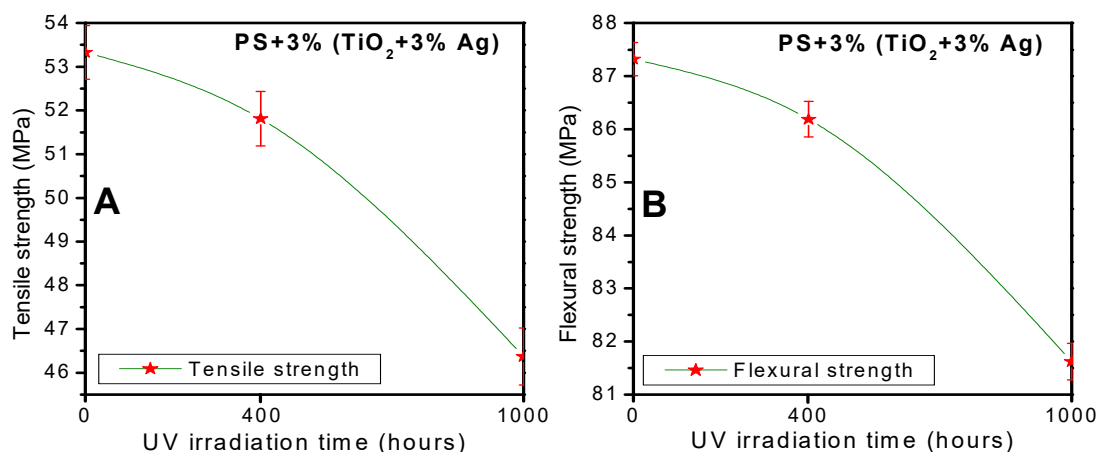

Figure 7.8.2. *Tensile (A) and flexural (B) strengths of PS-3%(TiO$_2$-3% Ag) composites exposed to UV radiation for 0, 400 and 1000 h.*

A comparison of tensile and flexural strengths of PS-TiO$_2$-metal and PS-TiO$_2$ composites are graphically represented in figure 7.8.1. It could be seen that the mechanical strengths of PS-TiO$_2$-metal composites were almost similar to that of PS-

TiO_2 composites. The mechanical strengths of PS-3%(TiO_2-3% Ag) were measured at UV irradiation time intervals of 0, 400 and 1000 hours (Figure 7.8.2). Tensile and flexural strengths of the composites decreased with the increase in UV irradiation time due to degradation.

7.5.5. Electrical properties

The value of dielectric breakdown (BDV) of PS-TiO_2-Ag was lower than that of PS-TiO_2 (Figure 7.9 A). Easier passage of electric charge across the polymer matrix in the presence of conducting Ag metal explains the observation. PS-TiO_2-metal composites can be used in such applications where enhanced electrical conductivity is demanded. From figure 7.9 A, the decrease in BDV with respect to the increase in UV irradiation time could also be observed. The decrease in BDV upon UV irradiation suggests that the free movement of charged species formed as a consequence of photodegradation is not hindered by Ag-doped TiO_2 across the polymer matrix.
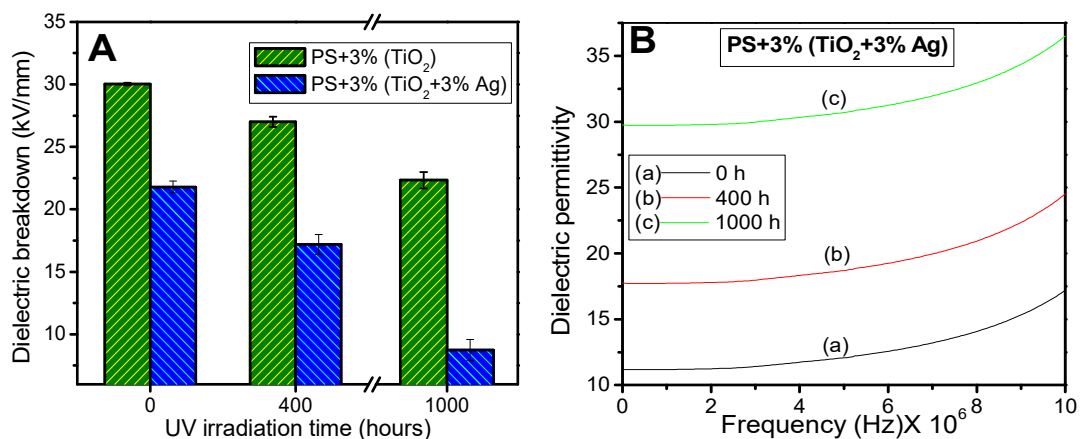

Figure 7.9. *Dielectric breakdown (A) and dielectric permittivity (B) of PS-(TiO_2-3% Ag) composite exposed to UV radiation for 0, 400 and 1000 h.*

Dielectric permittivity (ε_r) of PS-TiO_2-Ag composites was higher compared to that of PS-TiO_2 (Figure 7.9 B). The value of ε_r further increased upon UV irradiation. Formation of charged poles on UV irradiation is evident from this observation.

7.5.6. Thermogravimetric Analysis (TGA)

Thermogram of PS-(TiO_2-3% Ag) composite showed two stages of weight loss (Figure 7.10). The First stage of weight loss represents the water desorption of the composite. The second stage of weight loss resulting to a steep slope between 330 and

417° C represents the decomposition curve of the composite. The decomposition of the PS-(TiO$_2$-3% Ag) composite took place at an elevated temperature compared to that of PS-TiO$_2$ composite. This suggests that the thermal stability of PS-TiO$_2$-Ag composite was better compared to PS-TiO$_2$ composite. A decrease in the value of decomposition temperature was observed in the PS-(TiO$_2$-3% Ag) composite after 1000 hours of UV irradiation. The decomposition temperature was shifted to 311-396°C.
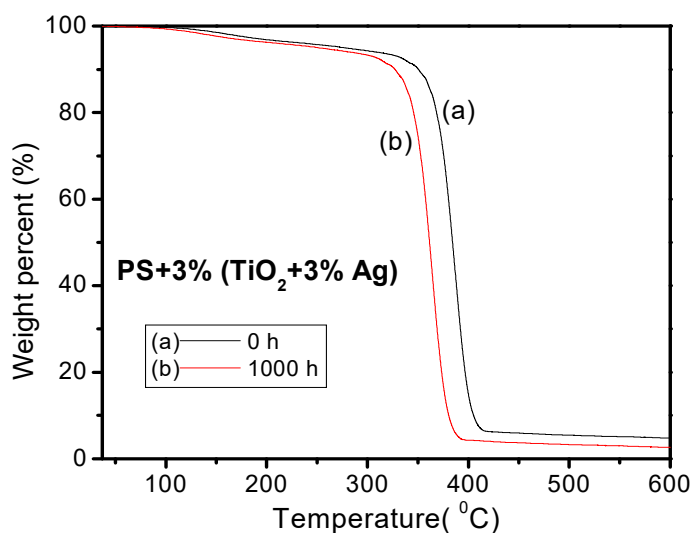

Figure 7.10. *TGA thermogram of PS-3%(TiO$_2$+3% Ag) composites before and after UV irradiation of 1000 h*
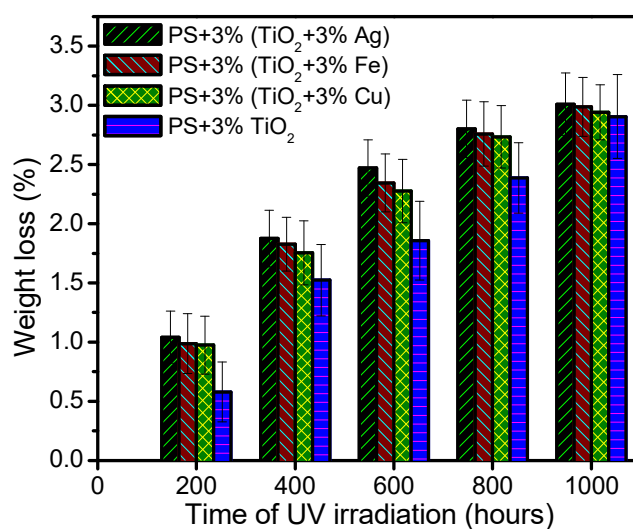
7.5.7. Weight loss

Figure 7.11. *Comparison of weight loss percentages of PS-TiO$_2$-metal composites at regular intervals of UV irradiation*

PS-TiO_2-metal composites underwent weight loss upon UV irradiation (Figure 7.11). All the PS-TiO_2-metal composites underwent enhanced weight loss compared to PS-TiO_2 composites. Maximum weight loss among the composites was observed in PS-TiO_2-Ag compared to others.

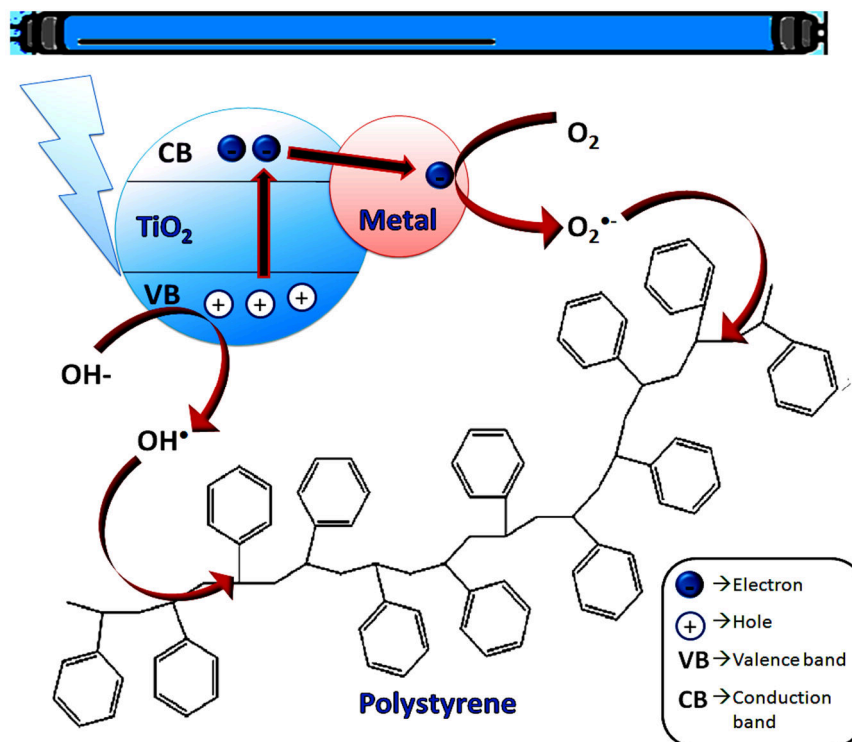## 7.6.   Mechanism of photocatalysis of TiO_2-metal composites

Figure 7.12. Pictorial representation of electron transfer from conduction band of TiO_2 to the doped transition metal, reducing the electron-hole recombination

An enhancement in the extent of photodegradation of PS-TiO_2-metal composites was observed compared to that of PS-TiO_2 composite. The increase in photocatalytic activity of TiO_2 upon metal doping was due to the fact that the transition metals block the recombination of photogenerated electrons and holes in TiO_2 upto an appreciable extent[40]. This charge pair separation efficiency is an outcome of improved charge transfer between the dopant metal and TiO_2[41].

Transition metal doping also reduces the bandgap of TiO_2 by altering the valence band maximum and conduction band minimum to new energy levels allowing the system to be photocatalytically active under radiations with lower energy[31]. The

decrease in bandgap energy was observed for Ag, Cu as well as Fe doped TiO_2 in our study as discussed earlier.

It was observed that Ag, Cu as well as Fe doped TiO_2 were all efficient photocatalyts for the degradation of PS even at low metal concentrations (3%). There was no expected improvement in the photocatalytic efficiency of these catalysts at higher concentration of metals (10% and 30%). Even though transition metals decreases the electron-hole recombination within TiO_2, higher concentration of metals may result in the formation of recombination centers which facilitate the charge recombination[42].

TiO_2-metal composites with higher metal doping percentages (10 and 30 mole percentages) existed predominantly in the rutile phase. Anatase TiO_2 is a better photocatalyst compared to rutile TiO_2[43]. PS loaded with TiO_2-10% and TiO_2-30% metals consisting of predominant rutile phase should not undergo better photodegradation compared to PS-(TiO_2-3% metal). This fact was in accordance with our observation. It has also been reported that even though anatase phase TiO_2 is photocatalytically more active than rutile phase, their mixed phase exhibited superior visible light induced photocatalytic activity. The heterojunctions formed as a result of mixing of the two phases is responsible for this[44,45]. In this point of view, the photodegradation of PS under visible light using TiO_2-metal composites with higher percentage of metal doping promises a future scope in research.

7.7. Conclusions

TiO_2 doped with 3, 10 and 30 mole percentages of Ag, Cu and Fe was prepared through sol-gel method. At a fixed calcination temperature of 400° C, the percentage of rutile phase increased and anatase phase decreased in the composites with respect to the increase in metal percentage. SEM images revealed that all the TiO_2-metal composites existed as spherical particles. The average diameters of TiO_2-3% Cu, TiO_2-3% Fe and TiO_2-3% Ag particles were ~125 nm, 85 nm and 50 nm respectively. The bandgap energies of all the composites decreased as the percentage of metal doping increased. PS loaded with TiO_2-metal composites underwent enhanced photo-oxidative degradation with deterioration in mechanical properties compared to PS-TiO_2 composites on UV exposure. The BDV of the PS-TiO_2-metal composites were

lower compared to PS-TiO₂ composites due to incorporation of conductive metals. Thermal stability of the composites was superior compared to PS-TiO2. Dielectric permittivity of the PS-TiO₂-metal composites was higher compared to PS-TiO₂. UV irradiated PS-TiO₂-metal composites also showed decreased thermal stability. BDV of the composites decreased and the dielectric permittivity increased upon UV irradiation. A notable observation made from the photodegradation studies was that the PS-TiO₂-metal composites with 3% metal underwent better photodegradation compared to that of 10 and 30% metal. Out of Ag, Cu and Fe doped TiO₂ photocatalysts, better photodegradation of PS was exhibited by Ag doped TiO₂ under UV irradiation.

References

1. Huang, F., Yan, A. & Zhao, H. Influences of doping on photocatalytic properties of TiO2 photocatalyst. *Semicond. Photocatal. Mech. Appl. Cao, W., Ed* 31–80 (2016).
2. Fan, W.-Q. *et al.* Titanium dioxide macroporous materials doped with iron: synthesis and photo-catalytic properties. *CrystEngComm* **16**, 116–122 (2014).
3. Chang, S. & Liu, W. The roles of surface-doped metal ions (V, Mn, Fe, Cu, Ce, and W) in the interfacial behavior of TiO2 photocatalysts. *Appl. Catal. B Environ.* **156–157**, 466–475 (2014).
4. Umebayashi, T., Yamaki, T., Itoh, H. & Asai, K. Analysis of Electronic Structures of 3D Transition Metal-Doped TiO2 Based on Band Calculations. *J. Phys. Chem. Solids* **63**, 1909–1920 (2002).
5. Ishii, M. *et al.* Roles of Electrons and Holes in the Luminescence of Rare-Earth-Doped Semiconductors. *Electron. Commun. Japan* **96**, 1–7 (2013).
6. Li, X. Z., Li, F. B., Yang, C. L. & Ge, W. K. Photocatalytic activity of WOx-TiO2 under visible light irradiation. *J. Photochem. Photobiol. A Chem.* **141**, 209–217 (2001).
7. Song, H., Jiang, H., Liu, X. & Meng, G. Efficient degradation of organic pollutant with WOx modified nano TiO2 under visible irradiation. *J. Photochem. Photobiol. A Chem.* **181**, 421–428 (2006).
8. Khairy, M. & Zakaria, W. Effect of metal-doping of TiO2 nanoparticles on their photocatalytic activities toward removal of organic dyes. *Egypt. J. Pet.* **23**, 419–426 (2014).
9. Guayaquil-Sosa, J. F., Serrano-Rosales, B., Valadés-Pelayo, P. J. & de Lasa, H. Photocatalytic hydrogen production using mesoporous TiO2 doped with Pt. *Appl. Catal. B Environ.* **211**, 337–348 (2017).
10. Lavorato, C. *et al.* Pd/TiO2 doped faujasite photocatalysts for acetophenone transfer hydrogenation in a photocatalytic membrane reactor. *J. Catal.* **353**, 152–161 (2017).
11. Jin, C. *et al.* Effects of single metal atom (Pt, Pd, Rh and Ru) adsorption on the photocatalytic properties of anatase TiO2. *Appl. Surf. Sci.* **426**, 639–646 (2017).
12. Hossain, M. A. *et al.* Synthesis of Fe- or Ag-doped TiO2–MWCNT nanocomposite thin films and their visible-light-induced catalysis of dye degradation and antibacterial activity. *Res. Chem. Intermed.* **44**, 2667–2683 (2018).
13. Zou, Z., Zhou, Z., Wang, H. & Yang, Z. Effect of Au clustering on ferromagnetism in Au doped TiO2 films: theory and experiments investigation. *J. Phys. Chem. Solids* **100**, 71–77 (2017).
14. Inturi, S. N. R., Boningari, T., Suidan, M. & Smirniotis, P. G. Visible-light-induced photodegradation of gas phase acetonitrile using aerosol-made transition metal (V, Cr, Fe, Co, Mn, Mo, Ni, Cu, Y, Ce, and Zr) doped TiO2. *Appl. Catal. B Environ.* **144**, 333–

342 (2014).

15. Sood, S., Umar, A., Mehta, S. K. & Kansal, S. K. Highly effective Fe-doped TiO2 nanoparticles photocatalysts for visible-light driven photocatalytic degradation of toxic organic compounds. *J. Colloid Interface Sci.* **450**, 213–223 (2015).

16. Birben, N. C. *et al.* Application of Fe-doped TiO2 specimens for the solar photocatalytic degradation of humic acid. *Catal. Today* **281**, 78–84 (2017).

17. Choudhury, B., Choudhury, A. & Borah, D. Interplay of dopants and defects in making Cu doped TiO2 nanoparticle a ferromagnetic semiconductor. *J. Alloys Compd.* **646**, 692–698 (2015).

18. Tripathi, A. K. *et al.* Structural, optical and photoconductivity of Sn and Mn doped TiO2 nanoparticles. *J. Alloys Compd.* **622**, 37–47 (2015).

19. Yadav, H. M. *et al.* Synthesis and visible light photocatalytic antibacterial activity of nickel-doped TiO2 nanoparticles against Gram-positive and Gram-negative bacteria. *J. Photochem. Photobiol. A Chem.* **294**, 130–136 (2014).

20. Khan, H. & Berk, D. Synthesis, physicochemical properties and visible light photocatalytic studies of molybdenum, iron and vanadium doped titanium dioxide. *React. Kinet. Mech. Catal.* **111**, 393–414 (2014).

21. Kaviyarasu, K. *et al.* In vitro cytotoxicity effect and antibacterial performance of human lung epithelial cells A549 activity of Zinc oxide doped TiO2 nanocrystals: Investigation of bio-medical application by chemical method. *Mater. Sci. Eng. C* **74**, 325–333 (2017).

22. Deng, L. *et al.* Synthesis, Characterization of Fe-doped TiO2 Nanotubes with High Photocatalytic Activity. *Catal. Letters* **129**, 513–518 (2009).

23. Tong, T., Zhang, J., Tian, B., Chen, F. & He, D. Preparation of Fe3+-doped TiO2 catalysts by controlled hydrolysis of titanium alkoxide and study on their photocatalytic activity for methyl orange degradation. *J. Hazard. Mater.* **155**, 572–579 (2008).

24. Jamalluddin, N. A. & Abdullah, A. Z. Reactive dye degradation by combined Fe(III)/TiO2 catalyst and ultrasonic irradiation: Effect of Fe(III) loading and calcination temperature. *Ultrason. Sonochem.* **18**, 669–678 (2011).

25. Wang, J. *et al.* Preparation of Fe-doped mixed crystal TiO2 catalyst and investigation of its sonocatalytic activity during degradation of azo fuchsine under ultrasonic irradiation. *J. Colloid Interface Sci.* **320**, 202–209 (2008).

26. Zhu, J., Zheng, W., He, B., Zhang, J. & Anpo, M. Characterization of Fe–TiO2 photocatalysts synthesized by hydrothermal method and their photocatalytic reactivity for photodegradation of XRG dye diluted in water. *J. Mol. Catal. A Chem.* **216**, 35–43 (2004).

27. Ambrus, Z. *et al.* Synthesis, structure and photocatalytic properties of Fe(III)-doped TiO2 prepared from TiCl3. *Appl. Catal. B Environ.* **81**, 27–37 (2008).

28. Hamadanian, M., Reisi-Vanani, A. & Majedi, A. Synthesis, characterization and effect of calcination temperature on phase transformation and photocatalytic activity of Cu,S-codoped TiO2 nanoparticles. *Appl. Surf. Sci.* **256**, 1837–1844 (2010).

29. Li, L. *et al.* Photocatalytic nitrate reduction over Pt–Cu/TiO2 catalysts with benzene as hole scavenger. *J. Photochem. Photobiol. A Chem.* **212**, 113–121 (2010).

30. Wang, S., Meng, K. K., Zhao, L., Jiang, Q. & Lian, J. S. Superhydrophilic Cu-doped TiO2 thin film for solar-driven photocatalysis. *Ceram. Int.* **40**, 5107–5110 (2014).

31. Mathew, S. *et al.* Cu-doped TiO2: Visible light assisted photocatalytic antimicrobial activity. *Appl. Sci.* **8**, 2067 (2018).

32. Sobana, N., Muruganadham, M. & Swaminathan, M. Nano-Ag particles doped TiO2 for efficient photodegradation of Direct azo dyes. *J. Mol. Catal. A Chem.* **258**, 124–132 (2006).

33. Sobana, N., Selvam, K. & Swaminathan, M. Optimization of photocatalytic degradation conditions of Direct Red 23 using nano-Ag doped TiO2. *Sep. Purif. Technol.* **62**, 648–653 (2008).

34. Sahoo, C., Gupta, A. K. & Pal, A. Photocatalytic degradation of Crystal Violet (C.I. Basic Violet 3) on silver ion doped TiO2. *Dye. Pigment.* **66**, 189–196 (2005).

35. Kondo, M. M. & Jardim, W. F. Photodegradation of chloroform and urea using Ag-loaded titanium dioxide as catalyst. *Water Res.* **25**, 823–827 (1991).
36. Suwarnkar, M., Dhabbe, R., Kadam, A. & Garadkar, P. K. M. Enhanced photocatalyticactivityofAgdopedTiO2 nanoparticles synthesized byamicrowaveassistedmethod. *Ceram. Int.* **40(2014)**, 5489–5496 (2013).
37. Luu, C. L., Nguyen, Q. T. & Ho, S. T. Synthesis and characterization of Fe-doped TiO 2 photocatalyst by the sol – gel method. *Adv. Nat. Sci. Nanosci. Nanotechnol.* **015008**, 1–6
38. Byrne, C., Fagan, R., Hinder, S., McCormack, D. E. & Pillai, S. C. New approach of modifying the anatase to rutile transition temperature in TiO2 photocatalysts. *RSC Adv.* **6**, 95232–95238 (2016).
39. Mogal, S. I. *et al.* Single-Step Synthesis of Silver-Doped Titanium Dioxide : In fl uence of Silver on Structural , Textural , and Photocatalytic Properties. *Ind. Eng. Chem. Res.* **53**, 5749−5758 (2014).
40. Behnajady, M. A., Modirshahla, N., Shokri, M. & Rad, B. Enhancement of photocatalytic activity of TiO2 nanoparticles by silver doping: photodeposition versus liquid impregnation methods. (2008).
41. Bagheri, S., Ramimoghadam, D., Yousefi, A. T. & Hamid, S. B. A. Synthesis, characterization and electrocatalytic activity of silver doped-titanium dioxide nanoparticles. *Int. J. Electrochem. Sci* **10**, 3088–3097 (2015).
42. Sung-Suh, H. M., Choi, J. R., Hah, H. J., Koo, S. M. & Bae, Y. C. Comparison of Ag deposition effects on the photocatalytic activity of nanoparticulate TiO2 under visible and UV light irradiation. *J. Photochem. Photobiol. A Chem.* **163**, 37–44 (2004).
43. Luttrell, T. *et al.* Why is anatase a better photocatalyst than rutile? - Model studies on epitaxial TiO2 films. *Sci. Rep.* **4**, 4043 (2014).
44. El-Sheikh, S. M. *et al.* High performance sulfur, nitrogen and carbon doped mesoporous anatase–brookite TiO2 photocatalyst for the removal of microcystin-LR under visible light irradiation. *J. Hazard. Mater.* **280**, 723–733 (2014).
45. Etacheri, V., Seery, M. K., Hinder, S. J. & Pillai, S. C. Nanostructured Ti1-xSxO2-yNy Heterojunctions for Efficient Visible-Light-Induced Photocatalysis. *Inorg. Chem.* **51**, 7164–7173 (2012).